MXene-reinforced water insensitive self-healing piezoelectric nanogenerator for ambient and aquatic mechano-pressure sensing

Sun, Ting-Wang; Venkatesan, Manikandan; Hsu, Yung-Chi; Chandrasekar, Jayashree; Chen, Wei-Cheng; Bénas, Jean-Sébastien; Liang, Fang-Cheng; Rwei, Alina Y.; Kuo, Chi-Ching; More Authors

DOI
10.1016/j.nanoen.2024.110416

Publication date
2025

Document Version
Final published version

Published in
Nano Energy

Nano Energy 133 (2025) 110416

Contents lists available at ScienceDirect

Nano Energy

journal homepage: www.elsevier.com/locate/nanoen

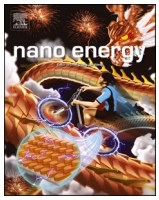

MXene-reinforced water insensitive self-healing piezoelectric nanogenerator for ambient and aquatic mechano-pressure sensing

Ting-Wang Sun [a,1], Manikandan Venkatesan [a,1], Yung-Chi Hsu [a,1], Jayashree Chandrasekar [a], Wei-Cheng Chen [a,b,c], Jean-Sébastien Bénas [a], Chia-Jung Cho [d], Ja-Hon Lin [e], Fang-Cheng Liang [a,*], Alina Y. Rwei [f,*], Chi-Ching Kuo [a,c,**]

[a] Department of Molecular Science and Engineering, Institute of Organic and Polymeric Materials, National Taipei University of Technology, Taipei 10608, Taiwan, ROC
[b] Department of Chemical Engineering, National Taiwan University, Taipei 10617, Taiwan, ROC
[c] Advanced Research Center for Green Materials Science and Technology, National Taiwan University, Taipei 10617, Taiwan, ROC
[d] Institute of Biotechnology and Chemical Engineering, I-Shou University, Kaohsiung 84001, Taiwan, ROC
[e] Department of Electro-Optical Engineering, National Taipei University of Technology, Taipei 106, Taiwan, ROC
[f] Department of Chemical Engineering, Delft University of Technology, Delft 2629 HZ, the Netherlands

ARTICLE INFO

Keywords:
MXene
Self-healing
Piezoelectric nanogenerator
Underwater sensing

ABSTRACT

The development of soft electronic devices capable of autonomous self-healing (SH) holds immense potential across various endeavours, promising to revolutionize product durability, reliability, and maintenance practices. Despite some progress has been made, underwater stable SH continues to be an active area of research. Herein, SH polymer PDMS-$MDI_{0.4}$-$TFB_{0.6}$ (SHP) with excellent mechanical property was composited with MXene to investigate the piezoelectric nature under various circumstance. By leveraging MXene into SHP not only improves the material properties of mechanical stress but also permittivity of the elastomer. Thus, MXene incorporated SHP (mSHP) induce high polarized charges under mechanical pressure. The fabrication of mSHP piezoelectric nanogenerator (mSHP-PENG) device via spray coating AgNWs on the surface forms ohmic contact, which facilitate high sensitivity and flexibility. Nevertheless, the generated piezoelectricity (30 V, 4.2 μA: 3 Hz) upon mechanical pressure gives maximum power density of 128 $\mu W/m^2$ indicating that our device can act as a reliable power source for portable electronic gadgets. In addition, SHP with amphiphilic functional groups sustain the original shape even after immerse into water for so long. Taking this into account, our device undergoes effective deformation even at low pressures, thus render to fabricate touch sensitive piezo-switches for both atmospheric and aquatics environments.

1. Introduction

Evaluation of wearable biomechanical sensors that can transduce human biophysical motion into electrical signals has gained extensive attention due to their ability towards human-machine interfaces, smart robotics, electronic E-skins, and healthcare monitoring [1–5]. Especially, piezoelectric materials have proven to be excellent in the field of bio-motion sensors because internal charge polarization upon mechanical deformation exhibited high sensitivity, thus rendering high amplitude signals as compared with the other resistive type and capacitive type sensors. In the development of piezoelectric sensors, there are many advancements have been made including high sensitivity, flexibility and long-time durability etc, [6]. This added additional feature brings piezoelectric research to the next level. Despite the increasing popularity of wearable electronics, concerns about their durability, sustainability, and waterproofing persist [7–9]. Therefore, identifying suitable materials for all the circumstances has become a critical issue. Developing wearable devices that incorporate SH capabilities and waterproofing is essential to ensure their long-term reliability and operation in challenging environments.

* Corresponding authors.
** Corresponding authors at: Department of Molecular Science and Engineering, Institute of Organic and Polymeric Materials, National Taipei University of Technology, Taipei 10608, Taiwan, ROC.
E-mail addresses: frank62112003@mail.ntut.edu.tw (F.-C. Liang), A.Y.Rwei@tudelft.nl (A.Y. Rwei), kuocc@mail.ntut.edu.tw (C.-C. Kuo).
[1] T.-W. Sun, M. Venkatesan, and Y.-C. Hsu contributed equally to this work.

https://doi.org/10.1016/j.nanoen.2024.110416
Received 8 September 2024; Received in revised form 22 October 2024; Accepted 27 October 2024
Available online 29 October 2024

In the past few decades, plenty of PENGs were reported by using PVDF and its copolymer as piezoelectric semi-crystalline polymers. So far, researchers discovered that enhancing the crystalline phase could improve the PENGs performance of PVDF [10]. Despite this, increasing the crystallinity by adding filler could reduce the agility of PVDF and increase the brittleness which is not recommended in wearable electronics. Therefore, discovering material with high flexibility and reusability even after several cycles can bring limelight to the current research. In this regard, the SH tendency of polymer can sustain the device from extreme pressures and cure damages similar to skin tissue [11]. Polydimethylsiloxane (PDMS) and its derivatives are commonly used as a host polymer to create soft electronic and actuators due to their high dielectric properties, and outstanding mechanical strength. Besides, PDMS is also a silicone elastomer which exhibits high flexibility, stretchability, free chain mobility, low glass transition temperature (-123℃), thermal stability, frost and UV resistance [12,13]. These features make PDMS elastomers a desirable material for encapsulating in electrical equipment. A tremendous effort has been made to fabricate autonomous self-repairing materials with increased durability to enhance the elastomer's visibility among researchers. For instance, Yang et al. [14] modified the 3-amino-propyl terminated polydimethylsiloxane (NH_2-PDMS) derivative using 4,4-methylene bisphenyl urea and isofordone biuret to fabricate a PENG pressure sensor. Although the PZT piezo ceramic incorporation gives stable output, the obtained voltage amplitude was limited to a smaller window, which indicates that the device was particularly designed for a lower pressure range. On the other hand, the water-assisted hydrogen bonding mechanism demonstrated faster SH; however, the water molecules were still a major concern because of swelling property deforms the structure of PENG under applied pressure. While Haick et al.[15] demonstrated a piezo-resistive sensor by using SH thermoplastic co-polymer for underwater pressure monitoring, but its pressure sensitivity in such applications is still underperformance. By taking all into account, it is important to design SH elastomer for all environmental adaptability.

MXene is a new class of 2D transition metal carbide obtained by wet chemical etching from MAX layered ternary carbide. It exhibits several advantages of non-centrosymmetric lattice structure, excellent conductivity, good water dispersibility, and reactive functional groups on the surface [16–18]. Owing to this MXene gained significant attention in various fields, including electromagnetic wave shielding, thermoelectric, electrochemical sensing, capacitors, photocatalysts and desalination seawater [19–22]. Especially, blending with the polymer can pave numerous advancements in energy harvesting and energy storage devices. Since the MXene nano/micro sheets attributes a large surface area and active functional groups, this forms a strong interconnection with polymer chains and provides sites to store the polarized charges at the shared interface with dielectric polymers [23].

This present work, demonstrates the mSHP-PENG energy-harvesting device for biomechanical pressure sensing in ambient and aquatic environments. By leveraging MXene, we improvised the charge polarization ability of as synthesized SHP for its versatile PENG application. With regards, the tensile and dielectric properties of SHP before and after incorporation of MXene were investigated. Intriguingly, the high surface functionality of MXene forms a strong interfacial interaction with SHP polymer chains, resulting in strengthening the chain entanglement, as well this crosslinking levitated the water insensitivity of SHP that can sustain its original shape. In addition, the high surface area of MXene helps to store the induced charges thereby the capacitance of SHP increased. Interestingly, the water sustainity and self-repairing nature of our PENG device extend its application to underwater pressure sensing. Therefore, our high sensitive piezo-pressure sensors demonstrated the ambient and aquatics environment pressure sensing.

2. Result and discussion

As described in the Fig. S1, the water insensitive, biocompatible SHP was synthesized via a one-pot two step approach. Firstly, the bis(3-aminopropyl)-terminated PDMS (H_2N-PDMS-NH_2) was blended with MDI and TFB composites to form a covalent reversible imine bond and hydrogen bond (PDMS-MDI $_{0.4}$ -TFB $_{0.6}$; Detail mechanism was discussed in the previous work). As synthesized SHP has proved to be used as a flexible substrate for the biocompatible e-skin electronic devices. Interestingly, MXene incorporation into SHP not only improves its capacitance and charge polarization but also cross-linkage with SHP enhances the mechanical toughness which sustains the shape of mSHP-PENG upon mechanical pressure. Fig. 1(a) shows the synthesis of MXene via the acid etching process, along with FE-SEM and its corresponding EDS (Fig. S3) analysis showing the multilayer structure of MXene that the Al layer is completely removed from the MAX phase. Consecutively, Fig. 1(b) shows the MXene powder being added to the SHP and subjected to ultra-sonication to ensure uniform mixing, the interaction of MXene with SHP is illustrated in Fig. S2. Then the distributed polymer solution was perfectly shaped using a PTFE mould. Then, the mSHP-PENG with sandwich structure is achieved by spraying Ag NWs on flat surfaces, and copper tape is used for extension. Lastly, a thin SHP was coated on the electrodes to complete the mSHP-PENG device encapsulation (Fig. 1(c)). The digital photographic image shows our high-pressure sensitive mSHP-PENG device.

X-ray diffraction (XRD) and Raman spectroscopy were used to characterize the MXene structure. For a better understanding of MXene formation XRD peak patterns of MAX phase and MXene is displayed in Fig. 2(a). It could be clearly seen that the Ti_3AlC_2 showed (002) diffraction peak at $2\theta \approx 9.6^{\circ}$, however after acid treatment, the (002) diffraction peak was shifted to a lower angle at $2\theta \approx 6.4^{\circ}$ and the most intense peak of Ti_3AlC_2 at $2\theta \approx 39^{\circ}$ corresponding to Al disappears, confirming the formation of MXene. The XRD patterns of SHP and MXene composite materials in different concentrations (mSHP) show an increase in the intensity of (002) peak with an increase in the concentration of MXene as in Fig. S4 indicating a high degree of crystallinity. Compared with the pure MXene powder, the mSHP showed a lower diffraction angle for (002) peak at $2\theta \approx 6^{\circ}$due to the SHP polymer chain intercalation that can influence the structure of MXene spacing, also the functional group on the surface of MXene might interact with some atoms at SHP like H or O, which can easily expand the spacing between MXene interlayer. Fig. 2(b) shows the Raman spectroscopy of SHP, MXene and mSHP. PDMS show two most intense peaks between 2800 and 3000 cm^{-1} corresponding to the symmetric and antisymmetric stretching vibrations of CH_3 while the peak at 495 cm^{-1} corresponds to the symmetric Si–O–Si stretching [24]. The feature peaks of pure MXene lies between 100 and 800 cm^{-1} as in Fig. S4. The peak at 219 cm^{-1} is attributed to the out of plane ($A_{1\ g}$) vibrations of titanium and carbon atoms while 403 cm^{-1} corresponds to the in-plane (E_g) vibrations of surface groups attached to titanium atoms indicating the etching of Al as well as the vibrations of C and surface groups involved. Furthermore, the peaks in the region from 580 to 730 cm^{-1} represented the carbon vibrations ($A_{1\ g}$ and E_g). Moreover, two new peaks were observed in the spectrum from 1300 to 1700 cm^{-1} which are the characteristic carbon peaks of D-band and G-band [25,26]. As a result, an increase in the charge transfer ability of MXene, and enhanced material polarization effect in SHP can be attained. These results conclude the successful synthesis of mSHP composite. In order to understand the surface chemistry of MXene, SHP and mSHP XPS analysis was carried out and the results are shown in Fig. 2(c-h). In the C1s spectra of MXene (Fig. 2(c)) peaks corresponding to O═C-O, C-F, C-C/C═C, and C-Ti-O were observed at 290.8 eV, 287.6 eV, 284.5 eV, and 281.9 eV, respectively. The C-Ti-O is the signature signal that confirms the MXene formation. In the case of SHP (Fig. 2(d)), the peak corresponding to C-C/Si-C was observed at binding energy of 284.5 eV [27]. Subsequently, this C-C/Si-C from SHP and C-Ti-O peak of MXene was easily observed in the C1s pattern of mSHP (Fig. 2(e)), however, a shift in the binding energy from 281.9 eV to 283.1 eV was observed for C-Ti-O due to the high electronegativity of MXene that alters the electron density resulting in a

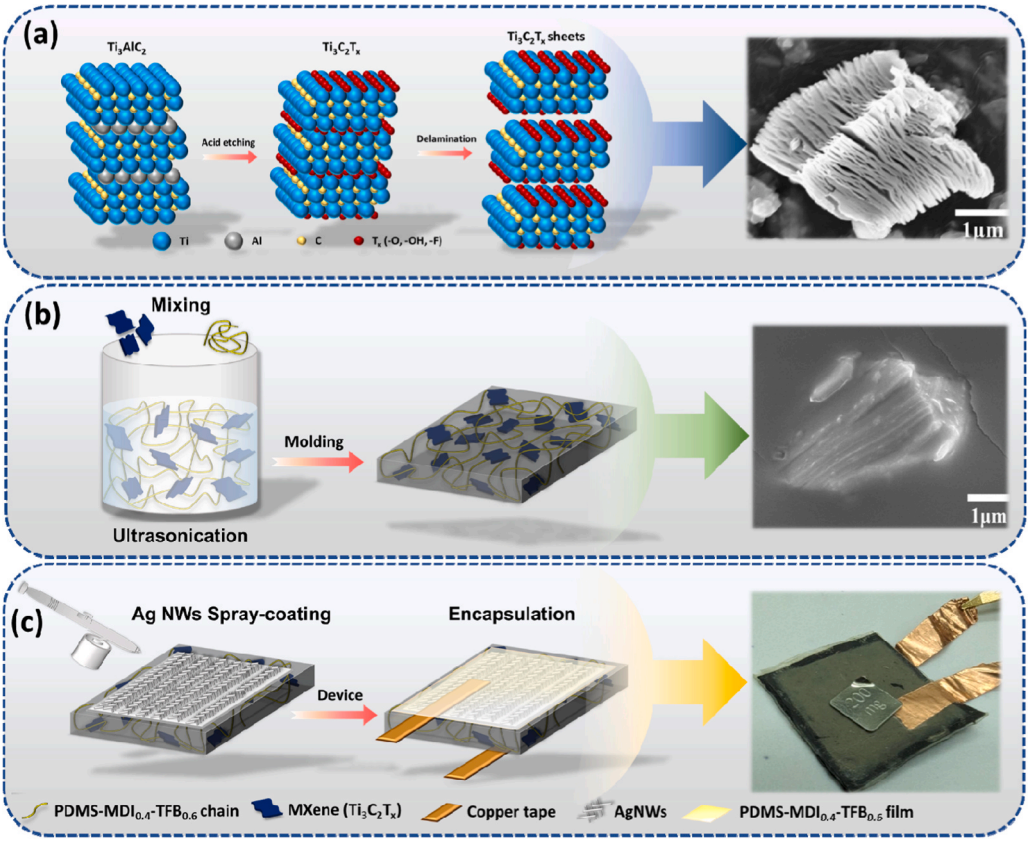

Fig. 1. (a) Schematic illustration of the MXene acid etching process corresponding FE-SEM surface morphology. (b) Preparation of MXene reinforced self-healing elastomer inset FE-SEM shows the incorporated MXene. (c) Illustrate the SHP-PENG device fabrication with photographic image.

positive shift in the binding energy. Furthermore, O1s spectra of MXene and SHP in Figs. 2(f) and 2(g) revealed peaks corresponding to H_2O, C-Ti-$(OH)_x$, C-Ti-O_x, and Ti-O at 538.0 eV, 535.4 eV, 532.9 eV, and 530.0 eV, respectively, with H_2O presumed to be residual water remaining in the MXene structure while SHP showed Si-O [27,28]. Interestingly, the O1s XPS of mSHP showed both Si-O and Ti-O with a shift in binding energy from 530.0 eV to 530.9 eV (Fig. 2(h)), which is due to the higher electronegativity of MXene compared to SHP. These results further confirm the successful formation of mSHP composite blending.

The piezoelectric working mechanism of mSHP-PENG was schematically illustrated in Fig. 3(a). When a mechanical force is applied to the device, the electric dipole charge balance of the dielectric polymer is disturbed, resulting in an electrostatic potential generated between the electrodes. During the periodic pressure-release cycle, the static potential charge imbalance causes the electron flow on the external circuit. MXene is a class of material with good electric conductivity with high surface area rendering the charge storage properties. Interestingly, MXene's non-centrosymmetric stacked atomic structure makes them high-directional piezoelectric materials. Further, charge accumulation at the MXene and SHP interface improved the capacitance and piezoelectric coefficient towards attaining a high electrical output. Moreover, Ag NWs spray coating forms ohmic contact on the surface of SHP providing reliable and complete energy transfer. To evaluate this charge polarization, the surface charge of SHP film with and without MXene was observed using a Kelvin probe force microscope (KPFM), this study measured the contact potential difference (CPD) between the probe tip and the sample contact surface. As shown in Fig. 3(b) we compared the CPD values obtained from the pristine SHP(+0.63 V); it is observed that the addition of MXene to the SHP (−0.57 V); shifted the surface charge potential toward negative values. The fact that SHP becomes more electronegative as a result of the addition of MXene is confirmed by a negative sign on the surface potential value (Fig. 3(c)). Briefly, PENG architecture is similar to the capacitor model in which the electric charges are separated by the piezoelectric effect. The Maxwell–Wagner–Sillars polarization effect describes that the gel-like SHP dielectric with conductive fillers can accumulate the charges at the interfaces this produces a strong polarization under pressure, whereby more static charges are induced on the electrode surface. On accounting for this interfacial polarization, we calculated the dielectric constant of SHP with various amounts of MXene doping at a frequency range between 1 Hz to 10 MHz. Fig. 3(d) demonstrates the permittivity of SHP film increased gradually upon MXene addition. Specifically, 25 wt% doped film shows an exponential increase in permittivity, it is obvious that conductive fillers yield significant relaxation at lower frequencies [29]. Whereas high concentration (30 wt%) causes charge leakage due to the reduced inter-particle distance that forms the conductive network of MXene. To further support this argument a finite element simulation was performed to qualitatively determine the stress and piezo-potential distribution in mSHP-PENG, in which the same mass fraction of MXene (25 wt%) loaded was identical to mSHP-PENG piezo-composite film. As revealed in Fig. 3(e), the stress deformation of the composite films and colour-coded piezo potential distribution were stimulated as downward bending (Model-I), and vertical compressive force (Model-II). Herein, composite film corners were fixed (two corners –Model-I, four corners –Model-II), and load pressure was applied on the film surfaces. In Model I, the downward bending stress causes an upward extrusion force, that results in the distribution of piezo-potentials at corners and at both ends in the middle. It is easier to understand that the application of bending force on the upper surface causes compression of both ends resulting in stretching of the middle portion in an curved structure. Whereas, in Model II, the compressive force applied from the vertical direction, shows more downward extrusion force resulting in the distribution of potential in a circular motion. The extrusion force causing a

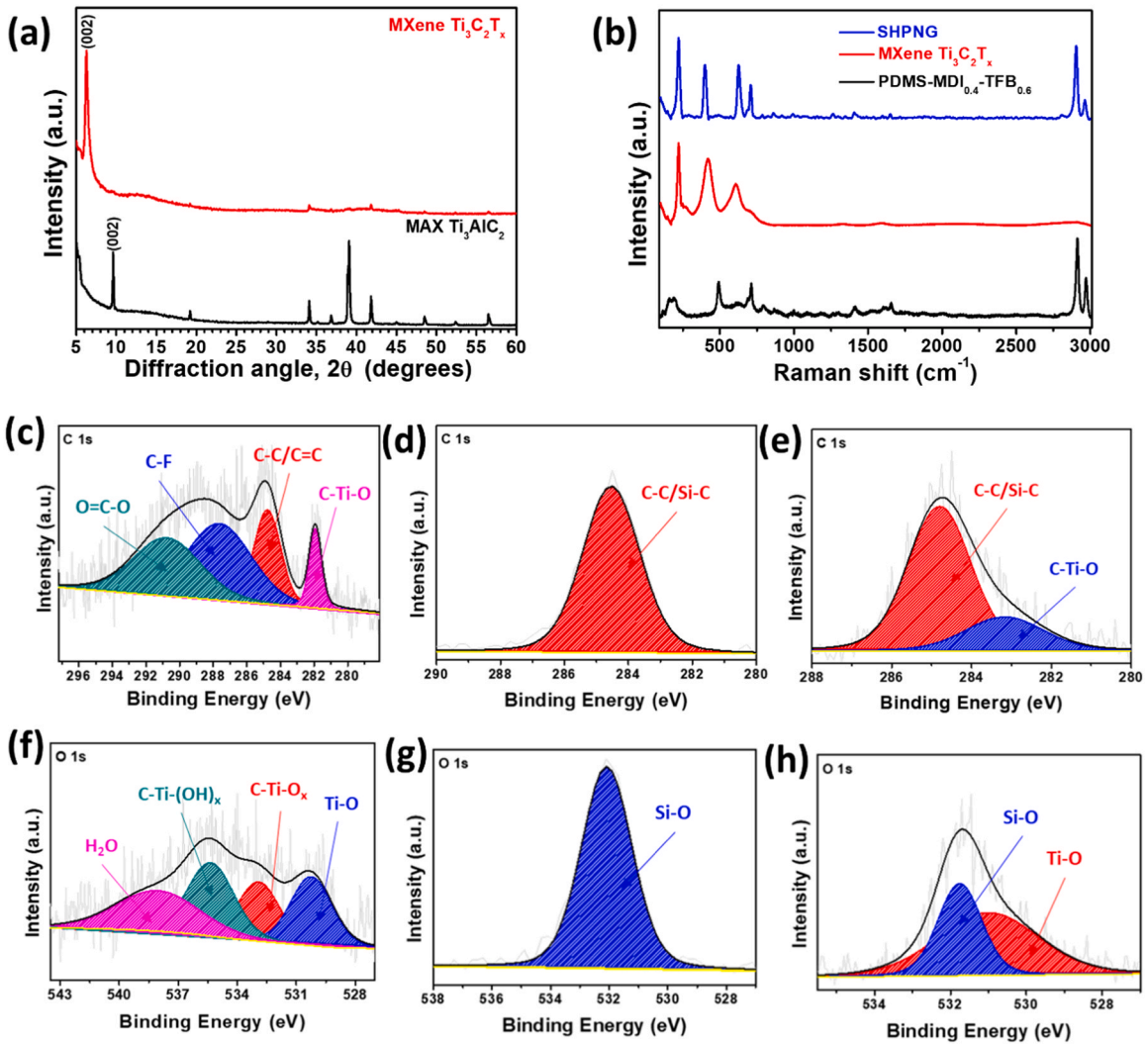

Fig. 2. (a) The XRD spectra of the MAX (Ti_3AlC_2) and MXene. (b) The Raman spectra of the SHP, MXene, and mSHP. The XPS spectra in the C 1 s of (c) MXene. (d) SHP. (e) mSHP. The XPS spectra in the O 1 s of (f) MXene. (g) SHP. (h) mSHP.

displacement enhances the piezo-potential as same as the variation of stress. In comparison between the two models, it can be concluded that the bending stress of the piezo-potential difference is lower (Model I) than the compressed state (Model II) which is in good agreement with the experimental results.

To optimize the electric output performance, the SHP composite film was fabricated with various amounts of MXene doping. It was found that the open-circuit voltage (Voc) and short-circuit current (Isc) gradually raised when the amount of MXene reached 25 wt% the Voc and Isc given the maximum output of 30 V and 4.2 μA under periodic pressure (Fig. 4 (a)). As we described earlier, when MXene loading exceeds the percolation limit the inter-particle distance is reduced and forms the MXene cluster, this creates a tunneling network that enables the charge neutralization with the counter electrode charges. Resulting in the weak charge polarization depleted the electric output, and a similar result is observed in the Isc plot (Fig. 4(b)). To understand the adaptability of the mSHP-PENG (hereafter denoted as $mSHP_{25}$-PENG) device under various imparting pressures, the optimized sample was repeatedly imparted with various frequencies, where the output data depicted a gradually increasing trend (Fig. 4(c) and (d)). This distinctive change is expected from the impedance of incorporated MXene. At low frequencies, the induced potential charges are easily neutralized by electrode charges; therefore, the electron flow in the circuit was reduced. Whereas at higher frequency ranges induced potential charges were not completely neutralized instead created a strong electric field to amplify the output performance of SHP−PENG. This frequency-dependent power output test results promise that our piezoelectric device can undergo continuous structural deformation without swelling or Ag NWs electrode network breakage. Furthermore, a switching polarity test was performed to prove the obtained charges were the result of piezo-potential differences under mechanical deformation and not from other phenomena. As depicted in Fig. 4(e), similar voltage peaks were observed in both forward and reverse bias connections. To further support this, a cross-sectional FE-SEM image of the $mSHP_{25}$-PENG device was taken after repeated finger imparting (Fig. S5). The image clearly demonstrates that the conductive Ag NWs layer remains well-adhered to the piezo-dielectric surface. This suggests that the possibility of forming any micro-sized gap between the Ag NWs and the SHP is minimal, thus excluding the possibility of additional frictional charge generation during finger imparting. Consecutively the device flexibility and compatibility was investigated upon various bending angles (30°, 60°, 90°, and 180°) in repeated modes of operation. With optimal agility and stretchability of $mSHP_{25}$-PENG, enable the sensor to provide reliable and continuous electric pulse information, which facilitates real-time monitoring of human health care as a wearable sensor (Fig. 4(f)).

Owing to the high charge polarity and flexibility our piezo device gives a fast response even for low-weight pressure. To demonstrate this pressure sensing ability, we measured the output voltage of our

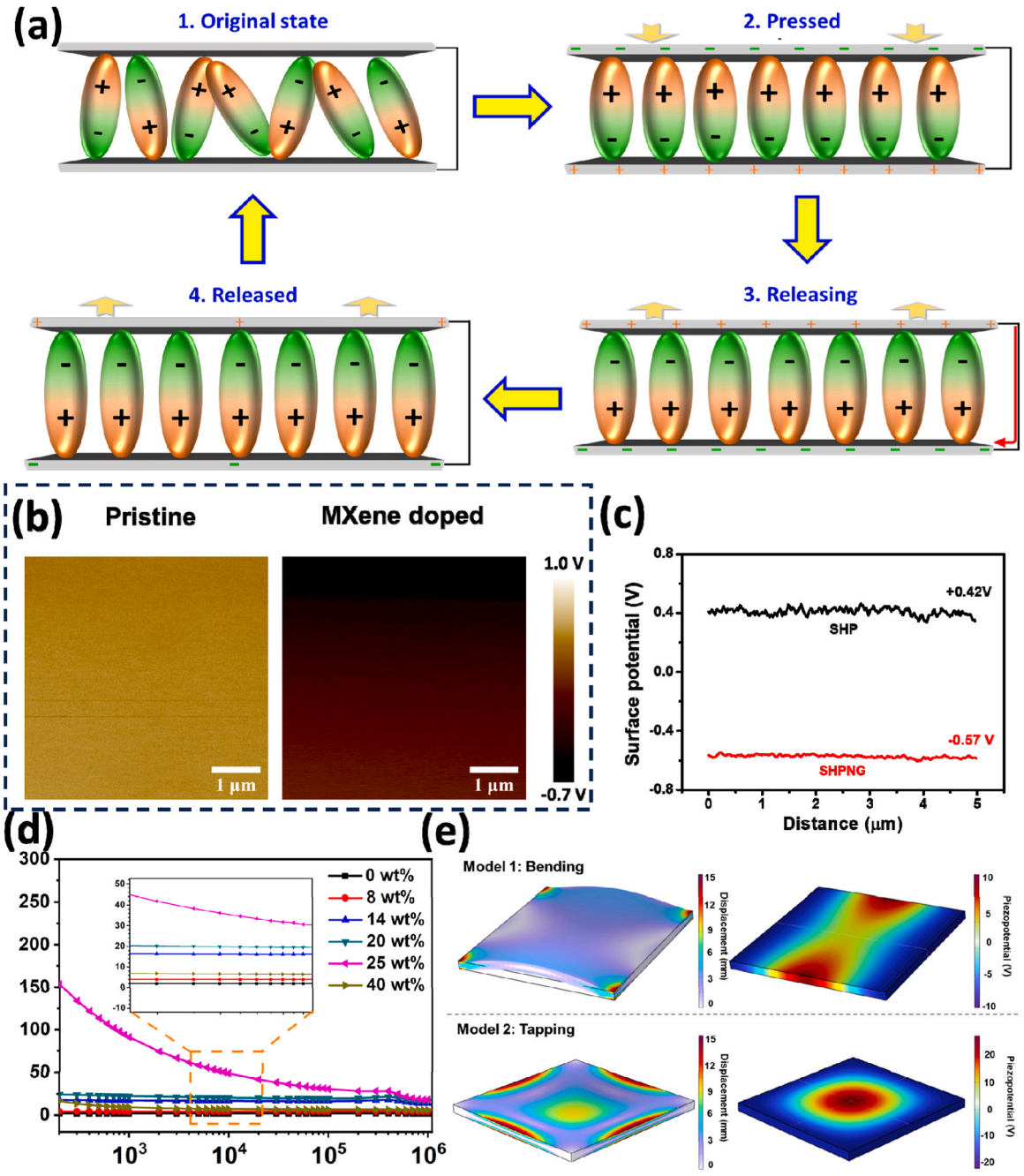

Fig. 3. (a) Illustrated the piezoelectric working mechanism upon compress- release cycle. (b) and (c) shows the KPFM surface charge distribution comparison of on SHP and mSHP. (d) Dielectric constant of various doping amount of MXene into SHP. (e) COMSOL elemental distribution of stress and surface charge potential image.

champion device by fixing the 30 g load object (Ball) to free fall on the device from various distances. The imparting kinetic force was estimated in supporting information. When the load weight hits the surface of $mSHP_{25}$-PENG from various distances, more potential charge is stimulated in the dielectric, which arises from imparting pressure. Resulted oscilloscope voltage peak intensity shows linear agreement with impacting pressure (Fig. 5(a), Inset image shows the imparting of free fall load on the PENG). The sensitivity value is defined as the relative voltage change upon the impacting pressure. As drawn linear slope gives a maximum sensitivity value of 0.53 V/kPa at mid-range force and optimal response to the low (0.056 V/kPa) and high-pressure region (0.017 V/kPa). Because SHP material is highly flexible and the spray-coated AgNWs electrode has ohmic contact with the polymer surface, therefore $mSHP_{25}$-PENG undergoes effective deformation and improves the result accuracy. To demonstrate the device performance in practical applications, various mass load objects (cotton bud, 1 g, 2 g, 5 g, and 10 g) voltage responses were studied in Fig. 5(b). As shown in Fig. 5(c), the voltage peak of the sensor with loading and unloading of the weight, and the corresponding loading peak response time was given 30 ms. This experimental result proves that the sensor has undergone effective deformation. To support this, we have compared the electrical behavior of our device with various piezoelectric devices in Table S1 (Supporting information). With a small active area, feasible structure and high-pressure response concluding that our $mSHP_{25}$-PENG can be integrated as a flexible mechanosensing device into healthcare pressure monitoring equipment.

In addition, to prove our PENG is a reliable power source for portable electronic equipment, it is essential to investigate how this $mSHP_{25}$-

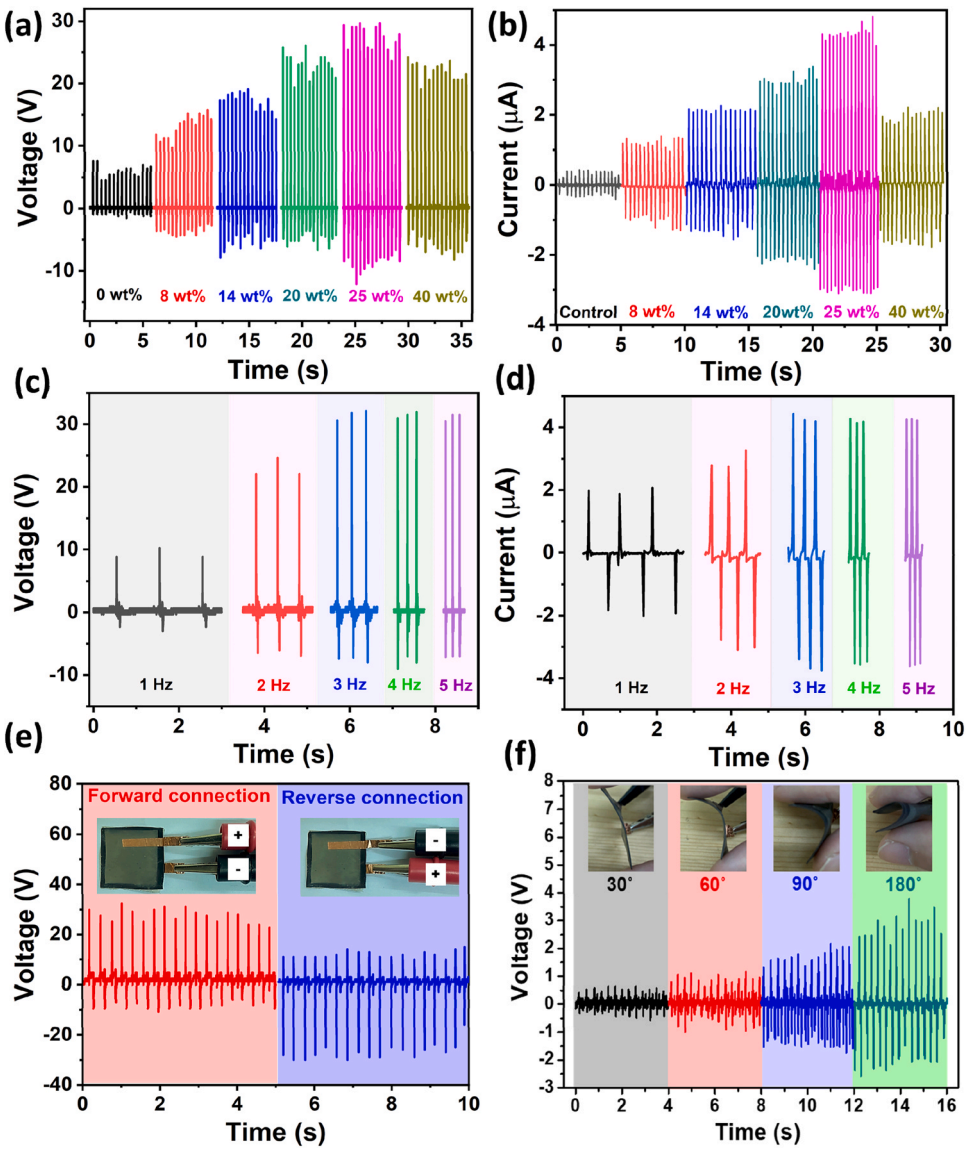

Fig. 4. (a) Shows the Voc of various MXene doped composite film. (b) Shows the Isc of various MXene doped composite film. (c-d) Shows the Voc of optimized sample $mSHP_{25}$-PENG at various frequency respectively. (e) Shows the forward and reverse bias voltage of the $mSHP_{25}$-PENG. (f) Shows Voc of various bending angle.

PENG can be made suitable in real-time applications. As shown in Fig. 5 (d) the $mSHP_{25}$-PENG device demonstrates the maximum power generation ability across various external load resistance from 1MΩ to 10MΩ. Such as the voltage increased proportionally upon resistance (R) increase and reached saturation point, thus proving that the $mSHP_{25}$-PENG attained maximum voltage at 8MΩ. Meanwhile, the evaluated power density provides their maximum intensity of 128 $\mu W/m^2$ with a similar resistor($PD = P/A$; $P - power, A - area$). Whereas at infinitesimal resistance the Isc value has become smaller, thus indicating the PD graph decline. Inset ohms law circuit indicates the $mSHP_{25}$-PENG device relation with V, I, and R. Such energy output can be satisfyingly utilized to charge a variety of commercial capacitors. Before storing the generated power into parallel plate capacitors, it required DC power rectification because the AC exhibits the capacitor charge and discharge simultaneously. Therefore, we designed $mSHP_{25}$-PENG device into a circuit where the capacitor is connected through the four-way bridge rectifier (Fig. 5(e)). Resulted rectified voltage is shown in Fig. 5(f), where the AC sign wave was fully converted into DC form. Followed by a series of (1 μF, 2.2 μF, 4.7 μF, 10 μF) capacitors charging was successfully demonstrated in Fig. 5(g) under 3 Hz frequency at constant pressure. Compared to other reported works our $mSHP_{25}$-PENG takes less time to charge the capacitors (Table S1; Supporting information), this affirms that our device has the potential to charge wearable smart garments in real-time applications. In addition, the long-term durability of the device was measured by applying constant force up to 1500 cycles (Fig. 5(h)). Interestingly, SH nature can cure scratches and damages on the surfaces quickly; such as, a completely packed device architecture can protect the electrodes peel-off. This suggesting excellent stability over a long period can put $mSHP_{25}$-PENG in the front line for wearable sensing applications. To demonstrate the real-time energy harvesting, a series of LED turn-on experiments were performed as shown in Fig. 5(i). This proves that our complete $mSHP_{25}$-PENG device can power up 5 LED lights instantly (Video S1).

Foreforth of this research mainly depends on the underwater SH mechanism, thus when water molecules contact with SHP assists in chain entanglement to heal the damages. Nevertheless, the amphiphilic nature of SHP mitigates the water ingress. Fig. 6(a) illustrates a scheme of the healing mechanism of SHP in an aquatic environment. The diffusion of water provokes the healing process as a combination of dynamic covalent imine bonds and H-bonds. The soft segment TFB

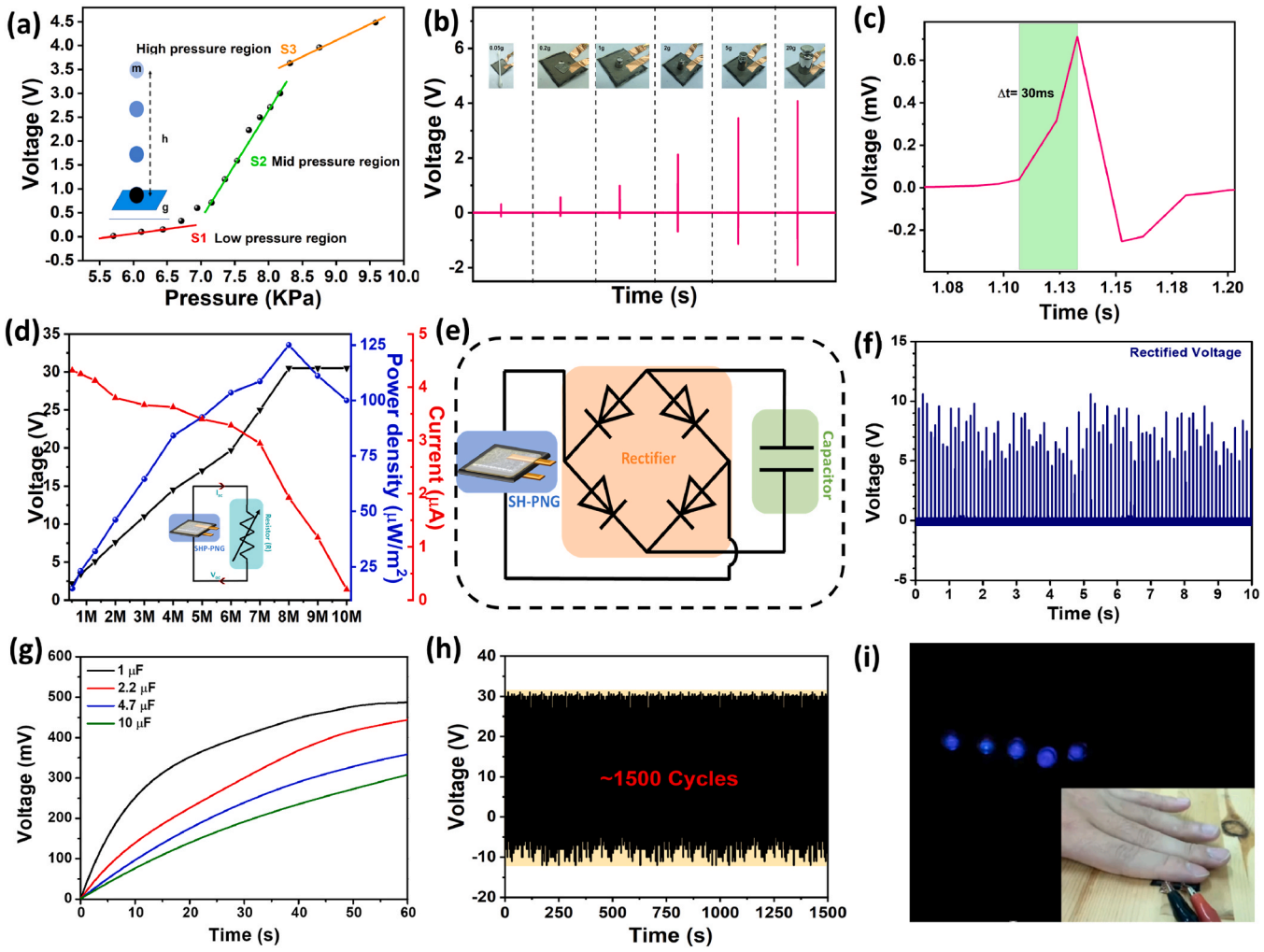

Fig. 5. (a) Shows the sensitivity graph of $mSHP_{25}$-PENG. (b) Voltage extrusion peak upon various load. (c) Shows voltage response time. (d) Reveals the power density of $mSHP_{25}$-PENG upon various external resistor. (e) Shows the integration of $mSHP_{25}$-PENG sample into circuit to convert the DC power. (f) Shows the rectified voltage through the bridge rectifier. (g) Capacitor charging. (h) Shows the voltage of life cycle test. (i) Indicate photograph image of the LED power up experiment.

undergoes an imine metathesis facilitating strain energy diffusion. While MDI hard segment forms a strong intermolecular H-bonds through urea based cross-linked network. The photographic image shown in Fig. 6(b) confirms that the scratch on the $mSHP_{25}$-PENG had completely disappeared on submersion into water. The observed seamless surface formation restores the AgNWs conductive network of $mSHP_{25}$-PENG. Furthermore, the complete SH has been further reflected by the voltage studies as shown in Fig. 6(b), thus the underwater healing process has completely restored the device performance. The tensile behavior of pristine SHP is investigated in Fig. 6(c), the result shows that water molecules enchant the tensile modulus more stretchable from (elongation 3911 %, maximum strain 0.55 MPa) to (elongation 4463 %, breaking strength 0.92 MPa). The deliberate incorporation of MXene reinforcement is found to enhance the mechanical stiffness and diminish the elasticity of SHP (elongation 2252 %, maximum strain 0.56 MPa). Nevertheless, even with the optimized ratio, the material still demonstrates promising healing capabilities. Notably, underwater healing of mSHP results in a substantial improvement in its tensile properties (elongation 3332 %, maximum strain 0.99 MPa), as illustrated in Fig. 6 (d). This enhancement is ascribed to the hydrophilic properties of MXene, which facilitate the interaction between water molecules and the polymer interface, thereby reinforcing chain entanglement. Fig. 6(e-f) shows the output voltage performance in air and under aquatic environments, these experimental results confirm that the induced polarized charges are only upon applied mechanical stimulation. Further to support this, we have demonstrated the underwater pressure sensing by integrating the $mSHP_{25}$-PENG device as a communicating key to the Arduino Uno (Video S2). This prototype experiment proves that our mechanosensitive device can be beneficial in forming an aquatic human-machine interface for transmitting signals from underwater to the surface world.

3. Conclusion

Concisely, we have designed an $mSHP_{25}$-PENG that sets a new trend and paves the way for underwater mechanical pressure switches. The incorporation of MXene with SHP exhibited outstanding mechanical and dielectric properties due to the strong interfacial interaction with the polymer chain. In addition, the non-centrosymmetric nature providing piezoelectric nature to MXene with SHP increased the capacitance of SHP by storing more induced charges resulting in a maximum output power density of 128 mW/m^2. At 25 wt% of MXene a high piezoelectric output of 30 V and 4.2 μA was attained. Interestingly, $mSHP_{25}$-PENG could sustain good performance even after 1500 cycles and can glow 5 blue LED lights. The excellent self-healing and its functioning in the water further guarantee its stable functioning in air and aquatic conditions. This research showcases significant advancements in underwater energy harvesting technology.

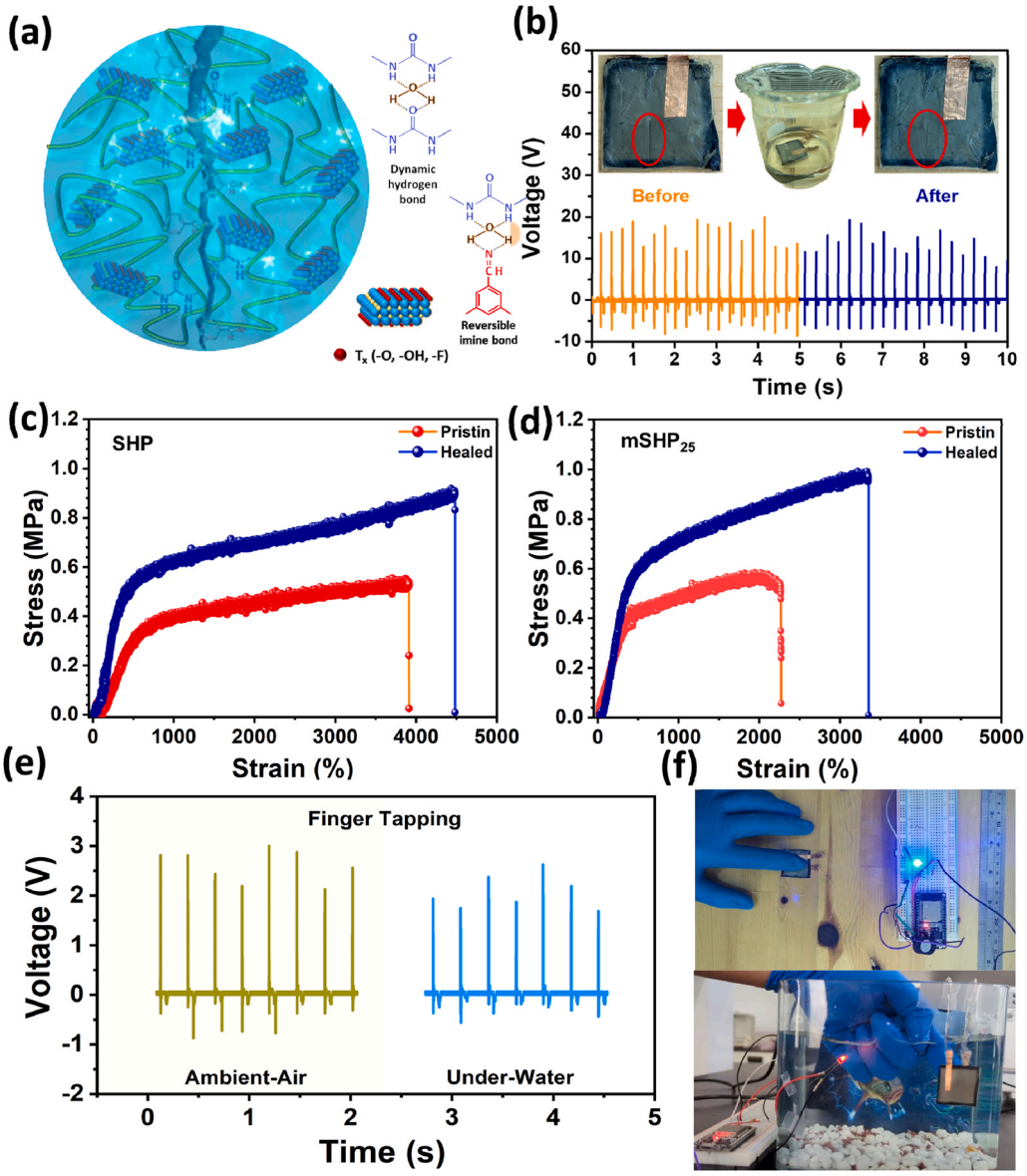

Fig. 6. (a) Schematic illustration of propagation of crack healing mechanism of SHP by reversible imine bond and hydrogen bonds with water molecule upon underwater healing process. (b) Voltage comparison of $mSHP_{25}$-PENG before and after crack and SH. (c) Stress- strain curves of SHP. (d) Stress-strain curve of (25 wt %) mSHP with cut healing. (e) Voltage comparison of $mSHP_{25}$-PENG in air and aquatic conditions. (f) Real-time demonstration of LED glowing by the device under normal and underwater.

4. Materials and methods

4.1. Materials

Ti_3AlC_2 (MAX) powder was purchased from Jilin 11 technology Co., Ltd, Polydimethylsiloxane (PDMS) was purchased from Gelest Inc., silver nanowires (AgNWs) was purchased from Zhejiang Kechuang Tech., Lithium fluoride (LiF, 99.98), Hydrochloric acid (HCl, 12 M), Ethanol (EtOH), chloroform ($CHCl_3$), Triformaldedhyde benzene (TFB), methylene diphenyl diisocyanate (MDI), were purchased from Sigma-Aldrich, All the materials were used without any purifications.

4.2. Preparation of Ti_3C_2 (MXene) and PDMS-$MDI_{0.4}$-$TFB_{0.6}$ Self-healing Polymer (SHP)

As described in the schematic, to etch the MAX phase, 0.8 g of LiF powder was added to 6 M HCl at 30℃ in a Teflon beaker and stirred at 350 rpm. Then, 0.5 g of MAX powder was slowly added to the solution and stirred for 24 hours. The resulting solution was washed with DI water and centrifuged at 3500 rpm for 5 minutes until the pH of the supernatant reached around 6–7 pH. The MXene was then dispersed in ethanol and sonicated for 1 hour in an ice bath to delaminate the nanosheets. Finally, the product was centrifuged at 5000 rpm for 30 minutes to collect the MXene nanosheets. The MXene powder was obtained by drying it overnight in a vacuum oven at 60℃. The SHP synthesis method is illustrated in Fig. S1 and was prepared using the method reported in our previous work [30].

4.3. Fabrication of mSHP-PENG device

The fabrication of the SHP-PENG device is as follows, 300 mg of SHP was dissolved in chloroform with different ratios of MXene which were 25 mg, 50 mg, 75 mg, 100 mg, and 200 mg, then stirred at room temperature for 24 hours. Subsequently, the mixture was poured into a 3 × 3 cm^2 area Teflon mould and sonicated to ensure the film was completely flat during the solvent evaporation. After 12 h of drying at

room temperature, a thin film was peeled off from the mold with a thickness of 0.25 mm. Then, the silver nanowire solution was loaded into a spray gun and evenly sprayed over an area of 2.5 × 2.5 cm^2 with a thickness of 0.005 mm on the surface of the film. The spray gun was positioned 10 cm above the material, and the spraying process was carried out for 5 minutes on both sides. A copper tape was stuck on the silver nanowires for electrical measurements.

4.4. Simulation

The piezoelectric charge induced and stress distribution of the SHP-PENG device were studied by using the COMSOL simulation multi-physics software (6.2 version). The rectangle geometry was modelled based on the SHP original values. The dielectric constant and mechanical strength of the blank material were employed based on 25 wt% of MXene. Further applied pressure and bending were performed as following the reference [31]. The number of corners was fixed depending on the model used, the top of the surface given as floating potential and the bottom of the surface given as ground.

4.5. Characterization

Fourier transform infrared spectroscopy (FT-IR) was performed on spectrum Two (PerkinElmer, UK) in the region of 4000–400 cm^{-1} with 16 scans at a resolution of 4 cm^{-1}. The XRD patterns of the prepared films were characterized by PAN alytical diffractometer S6 (X' Pert3 Powder). Raman spectrometer (LabRAM HR 800 UV; Horiba). A tensile test QC 508 (Cometech Testing Machines Co., Ltd., Taiwan) was conducted to determine the mechanical properties. The measurements were conducted at different loading rates (20 mm min^{-1}, 50–70 mm min^{-1}). Surface potential was observed using a Kelvin probe force microscope (KPFM Bruker-Dimension Icon) and an electrostatic voltmeter. A field emission scanning electron microscope (FE-SEM) was performed on an S4800 (HITACHI, Japan). X-ray photoelectron spectroscopy (XPS, Thermo Fisher Scientific Theta probe). The contact angle was measured using an FTA125 contact angle analysis system (FTA). Electrical performances such as the open-circuit voltage and short-circuit current were studied through Oscilloscope and Keithley 6500 respectively. The capacitance was collected using an LCR meter (Agilent E498E precision). Scale bar and fiber diameter were identified by ImageJ software.

CRediT authorship contribution statement

Manikandan Venkatesan: Writing – review & editing, Writing – original draft, Software, Methodology, Investigation, Formal analysis, Data curation. **Chi-Ching Kuo:** Writing – review & editing, Writing – original draft, Supervision, Software, Resources, Methodology, Investigation, Formal analysis, Data curation. **Ting-Wang Sun:** Writing – review & editing, Writing – original draft, Software, Methodology, Investigation, Formal analysis, Data curation. **Fang-Cheng Liang:** Methodology, Formal analysis, Data curation. **Alina Y. Rwei:** Writing – original draft, Supervision, Software, Formal analysis, Data curation. **Chia-Jung Cho:** Software, Formal analysis, Data curation. **Ja-Hon Lin:** Methodology, Investigation, Formal analysis, Data curation. **Wei-Cheng Chen:** Writing – original draft, Software, Methodology, Investigation, Formal analysis, Data curation. **Jean-Sébastien Bénas:** Software, Methodology, Investigation, Formal analysis, Data curation. **Yung-Chi Hsu:** Writing – original draft, Software, Methodology, Formal analysis, Data curation. **Jayashree Chandrasekar:** Software, Methodology, Formal analysis, Data curation.

Declaration of Competing Interest

The authors declare that they have no known competing financial interests or personal relationships that could have appeared to influence the work reported in this paper.

Acknowledgments

C.-C. Kuo acknowledges the financial support provided by the National Science and Technology Council (Contracts: NSTC 112–2221-E-027–003 -MY3, NSTC 113–2221-E-027–119 -MY3), and National Taipei University of Technology International Joint Research Project (NTUT-IJRP-112–02). This work was financially supported by the "Advanced Research Center for Green Materials Science and Technology" from the Featured Area Research Center Program within the framework of the Higher Education Sprout Project by the Ministry of Education (113L9006).

Appendix A. Supporting information

Supplementary data associated with this article can be found in the online version at doi:10.1016/j.nanoen.2024.110416.

Data Availability

Data will be made available on request.

References

[1] R.G. Ferreira, A.P. Silva, J. Nunes-Pereira, Current on-skin flexible sensors, materials, manufacturing approaches, and study trends for health monitoring: a review, ACS Sens. 9 (2024) 1104–1133, https://doi.org/10.1021/acssensors.3c02555.
[2] K.K. Das, B. Basu, P. Maiti, A.K. Dubey, Piezoelectric nanogenerators for self-powered wearable and implantable bioelectronic devices, Acta Biomater. 171 (2023) 85–113, https://doi.org/10.1016/j.actbio.2023.08.057.
[3] N.K. Das, S. Veeralingam, S. Badhulika, Zinc ferrite nanoparticle-based wearable piezoelectric nanogenerators as self-powered sensors to monitor human motion, ACS Appl. Nano Mater. 6 (2023) 13431–13442, https://doi.org/10.1021/acsanm.3c02085.
[4] S. Zeng, M. Zhang, L. Jiang, Z. Wang, H. Gu, J. Xiong, Y. Du, L. Ren, Wearable piezoelectric nanogenerators based on core–shell Ga-PZT@GaO x nanorod-enabled P(VDF-TrFE) composites, ACS Appl. Mater. Interfaces 14 (2022) 7990–8000, https://doi.org/10.1021/acsami.1c22877.
[5] H. Tabasum, N. Gill, R. Mishra, S. Lone, Wearable microfluidic-based e-skin sweat sensors, RSC Adv. 12 (2022) 8691–8707, https://doi.org/10.1039/D1RA07888G.
[6] M. Venkatesan, W.-C. Chen, C.-J. Cho, L. Veeramuthu, L.-G. Chen, K.-Y. Li, M.-L. Tsai, Y.-C. Lai, W.-Y. Lee, W.-C. Chen, C.-C. Kuo, Enhanced piezoelectric and photocatalytic performance of flexible energy harvester based on CsZn0.75Pb0.25I3/CNC–PVDF composite nanofibers, Chem. Eng. J. 433 (2022) 133620, https://doi.org/10.1016/j.cej.2021.133620.
[7] Q. Xu, Y. Tao, Z. Wang, H. Zeng, J. Yang, Y. Li, S. Zhao, P. Tang, J. Zhang, M. Yan, Q. Wang, K. Zhou, D. Zhang, H. Xie, Y. Zhang, C. Bowen, Highly flexible, high-performance, and stretchable piezoelectric sensor based on a hierarchical droplet-shaped ceramics with enhanced damage tolerance, Adv. Mater. (2024), https://doi.org/10.1002/adma.202311624.
[8] Y.-G. Kim, J.-H. Song, S. Hong, S.-H. Ahn, Piezoelectric strain sensor with high sensitivity and high stretchability based on kirigami design cutting, Npj Flex. Electron. 6 (2022) 52, https://doi.org/10.1038/s41528-022-00186-4.
[9] Y.-G. Kim, S. Hong, B. Hwang, S.-H. Ahn, J.-H. Song, Improved performance of stretchable piezoelectric energy harvester based on stress rearrangement, Sci. Rep. 12 (2022) 19149, https://doi.org/10.1038/s41598-022-23005-2.
[10] L. Zhang, S. Li, Z. Zhu, G. Rui, B. Du, D. Chen, Y. Huang, L. Zhu, Recent progress on structure manipulation of poly(vinylidene fluoride)-based ferroelectric polymers for enhanced piezoelectricity and applications, Adv. Funct. Mater. 33 (2023), https://doi.org/10.1002/adfm.202301302.
[11] Y. Zou, P. Tan, B. Shi, H. Ouyang, D. Jiang, Z. Liu, H. Li, M. Yu, C. Wang, X. Qu, L. Zhao, Y. Fan, Z.L. Wang, Z. Li, A bionic stretchable nanogenerator for underwater sensing and energy harvesting, Nat. Commun. 10 (2019) 2695, https://doi.org/10.1038/s41467-019-10433-4.
[12] E.-J. Chang, M.-F. Lin, Enhanced actuation performance of multiple stimuli responsive PDMS-based bilayer actuators by adding ionic liquid, Sens. Actuators B Chem. 404 (2024) 135300, https://doi.org/10.1016/j.snb.2024.135300.
[13] S.W. Kim, J.-H. Lee, H.J. Ko, S. Lee, G.Y. Bae, D. Kim, G. Lee, S.G. Lee, K. Cho, Mechanically robust and linearly sensitive soft piezoresistive pressure sensor for a wearable human–robot interaction system, ACS Nano 18 (2024) 3151–3160, https://doi.org/10.1021/acsnano.3c09016.
[14] M. Yang, J. Liu, D. Liu, J. Jiao, N. Cui, S. Liu, Q. Xu, L. Gu, Y. Qin, A fully self-healing piezoelectric nanogenerator for self-powered pressure sensing electronic skin, Research 2021 (2021), https://doi.org/10.34133/2021/9793458.
[15] M. Khatib, O. Zohar, W. Saliba, S. Srebnik, H. Haick, Highly efficient and water-insensitive self-healing elastomer for wet and underwater electronics, Adv. Funct. Mater. 30 (2020), https://doi.org/10.1002/adfm.201910196.

[16] D. Tan, C. Jiang, N. Sun, J. Huang, Z. Zhang, Q. Zhang, J. Bu, S. Bi, Q. Guo, J. Song, Piezoelectricity in monolayer MXene for nanogenerators and piezotronics, Nano Energy 90 (2021) 106528, https://doi.org/10.1016/j.nanoen.2021.106528.
[17] X. Pan, X. Yang, M. Yu, X. Lu, H. Kang, M.-Q. Yang, Q. Qian, X. Zhao, S. Liang, Z. Bian, 2D MXenes polar catalysts for multi-renewable energy harvesting applications, Nat. Commun. 14 (2023) 4183, https://doi.org/10.1038/s41467-023-39791-w.
[18] V. Shukla, The tunable electric and magnetic properties of 2D MXenes and their potential applications, Mater. Adv. 1 (2020) 3104–3121, https://doi.org/10.1039/D0MA00548G.
[19] L. Liang, C. Yao, X. Yan, Y. Feng, X. Hao, B. Zhou, Y. Wang, J. Ma, C. Liu, C. Shen, High-efficiency electromagnetic interference shielding capability of magnetic Ti 3C 2 T x MXene/CNT composite film, J. Mater. Chem. A. 9 (2021) 24560–24570, https://doi.org/10.1039/D1TA07781C.
[20] Y. Yang, Y. Xu, Q. Li, Y. Zhang, H. Zhou, Two-dimensional carbide/nitride (MXene) materials in thermal catalysis, J. Mater. Chem. A. 10 (2022) 19444–19465, https://doi.org/10.1039/D2TA03481F.
[21] W. Fan, Q. Wang, K. Rong, Y. Shi, W. Peng, H. Li, Z. Guo, B.Bin Xu, H. Hou, H. Algadi, S. Ge, MXene enhanced 3D needled waste denim felt for high-performance flexible supercapacitors, Nano-Micro Lett. 16 (2024) 36, https://doi.org/10.1007/s40820-023-01226-y.
[22] X. Liu, J. Tong, J. Wang, S. Lu, D. Yang, H. Li, C. Liu, Y. Song, BaTiO 3 /MXene/PVDF-TrFE composite films via an electrospinning method for flexible piezoelectric pressure sensors, J. Mater. Chem. C. 11 (2023) 4614–4622, https://doi.org/10.1039/D2TC05291A.
[23] J. Huang, X. Huang, P. Wu, One stone for three birds: one-step engineering highly elastic and conductive hydrogel electronics with multilayer MXene as initiator, crosslinker and conductive filler simultaneously, Chem. Eng. J. 428 (2022) 132515, https://doi.org/10.1016/j.cej.2021.132515.
[24] M.R. Gonçalves, F. Enderle, O. Marti, Surface-enhanced Raman spectroscopy of dye and thiol molecules adsorbed on triangular silver nanostructures: a study of near-field enhancement, localization of hot-spots, and passivation of adsorbed carbonaceous species, J. Nanotechnol. 2012 (2012) 1–15, https://doi.org/10.1155/2012/173273.
[25] M. Dong, Y. Hu, H. Zhang, E. Bilotti, N. Pugno, D. Dunstan, D.G. Papageorgiou, Micromechanics of Ti3C2Tx MXene reinforced poly(vinyl alcohol) nanocomposites, Compos. Part C. Open Access. 13 (2024) 100427, https://doi.org/10.1016/j.jcomc.2023.100427.
[26] F. Liu, A. Zhou, J. Chen, H. Zhang, J. Cao, L. Wang, Q. Hu, Preparation and methane adsorption of two-dimensional carbide Ti2C, Adsorption 22 (2016) 915–922, https://doi.org/10.1007/s10450-016-9795-8.
[27] K. Malecha, I. Gancarz, W. Tylus, Argon plasma-assisted PDMS–LTCC bonding technique for microsystem applications, J. Micromech. Microeng. 20 (2010) 115006, https://doi.org/10.1088/0960-1317/20/11/115006.
[28] Y. Cao, Q. Deng, Z. Liu, D. Shen, T. Wang, Q. Huang, S. Du, N. Jiang, C.-T. Lin, J. Yu, Enhanced thermal properties of poly(vinylidene fluoride) composites with ultrathin nanosheets of MXene, RSC Adv. 7 (2017) 20494–20501, https://doi.org/10.1039/C7RA00184C.
[29] A.Hisyam A. Razak, P. Szabo, A.L. Skov, Enhancement of dielectric permittivity by incorporating PDMS-PEG multiblock copolymers in silicone elastomers, RSC Adv. 5 (2015) 53054–53062, https://doi.org/10.1039/C5RA09708H.
[30] C. He, F. Liang, L. Veeramuthu, C. Cho, J. Benas, Y. Tzeng, Y. Tseng, W. Chen, A. Rwei, C. Kuo, Super tough and spontaneous water-assisted autonomous self-healing elastomer for underwater wearable electronics, Adv. Sci. 8 (2021), https://doi.org/10.1002/advs.202102275.
[31] H. Su, X. Wang, C. Li, Z. Wang, Y. Wu, J. Zhang, Y. Zhang, C. Zhao, J. Wu, H. Zheng, Enhanced energy harvesting ability of polydimethylsiloxane-BaTiO3-based flexible piezoelectric nanogenerator for tactile imitation application, Nano Energy 83 (2021) 105809, https://doi.org/10.1016/j.nanoen.2021.105809.